Paper D

Discretisation Schemes for Anisotropic Heterogeneous Media on Near-well Grids *

* Accepted for publication in Computational Geosciences
doi:10.1007/s10596-009-9167-5

Noname manuscript No.
(will be inserted by the editor)

Simulation of Anisotropic Heterogeneous Near-well Flow using MPFA Methods on Flexible Grids

S. S. Mundal · E. Keilegavlen · I. Aavatsmark

Received: date / Accepted: date

Abstract Control-volume multipoint flux approximations (MPFA) are discussed for the simulation of complex near-well flow using geometrically flexible grids. Due to the strong non-linearity of the near-well flow, a linear model will in general be inefficient. Instead, a model accounting for the logarithmic pressure behavior in the well vicinity is advocated. This involves a non-uniform refinement of the grid in radial direction. The model accounts for both near-well anisotropies and heterogeneities. For a full simulation involving multiple wells, this single-well approach can easily be coupled with the reservoir model. Numerical simulations demonstrate the convergence behavior of this model using various MPFA schemes under different near-well conditions for single phase flow regimes. Two-phase simulations support the results of the single phase simulations.

S. S. Mundal
Department of Mathematics,
Centre for Integrated Petroleum Research (CIPR),
University of Bergen,
P.O. Box 7800, N-5020 Bergen -Norway
Tel.: +47-55 58 48 79
Fax: +47-55 58 82 65
E-mail: sissel.mundal@cipr.uib.no

E. Keilegavlen
CIPR, Bergen -Norway
Tel.: +47-55 58 36 74
Fax: +47-55 58 82 65
E-mail: eirik.keilegavlen@cipr.uib.no

I. Aavatsmark
CIPR, Bergen -Norway
Tel.: +47-55 58 35 44
Fax: +47-55 58 82 65
E-mail: ivar.aavatsmark@cipr.uib.no

Keywords near-well modeling · control-volume discretization · anisotropy · heterogeneity

1 Introduction

In reservoir engineering, accurate well modeling is crucial for reliable fluid flow simulations. Reservoirs are managed through data accessed from the wells, and important well parameters, like the well flow rate and well bore pressure, are sensitive to the computational accuracy of near-well flow models.

In his papers of 1978 and 1983 [26,27], Peaceman introduced a way to relate the well bore pressure, the well block pressure and the well flow rate for both isotropic and anisotropic permeabilities, respectively, through a numerical productivity index. Among the assumptions for his derivation, is the restriction to 2D uniform rectangular grids in homogeneous media. Despite its limitation, the formula is still a widely used well model in reservoir simulation.

However, the key issue in numerical well simulations is the difference in reservoir scale and the well bore radius. Reservoir flow models do not fully capture the true flow behavior in the well vicinity. Grid blocks are generally on the scale of several tens of meters, whereas a typical well bore radius is on centimeter scale. Near-well regions are characterized as high-flow density regions, and the dominating flow pattern exhibits a radial-like nature with large pressure gradients, and for multiphase flow, large saturation gradients caused by high production rates. Skew or horizontal wells will also in general imply a strong effect of anisotropy and heterogeneities due to geological layering of the reservoirs. Hence, a near-well model should be flexible with regards to local

grid refinement and the handling of complex geological near-well structures.

Thus, contrary to the point sink/source Peaceman well model, we will impose a description of physical variables on the well bore boundary itself. By discretizing the well bore, a numerical well index need not be defined, and we allow for the use of locally refined flexible grids in the well vicinity. We are thus able to resolve the well geometry and improve the accuracy of the flow simulation. The finite well bore approach is well suited for studying coning behavior in single-well problems for multiphase flow. In full-field simulations, however, fine grids are computationally expensive and may lead to impractical restrictions on the time step size. Moreover, during the lifetime of a reservoir, wells are frequently being opened and shut-down for optimal production. Local grid refinements are thus superfluous in the vicinity of inactive wells. For active wells, the near-well dynamics can be upscaled utilizing a local fine grid around the well bore [34]. Furthermore, the windowing technique described in [22] is designed to supplement simulations on a global grid with local fine grids. This technique is adaptive both in time and space. Hence, it may remedy the CFL-restrictions due to local grid refinements near a well, whether the well is active or not. Our focus in this work is discretization techniques based on fine grids in the well vicinity. The issue of reducing the computational cost when applying these techniques in full-scale simulations, will not be further addressed here.

As the well singularity is the predominant driving force for the flow in the well vicinity, we seek a model which takes this logarithmic pressure behavior into account. It is commonly recognized that numerical schemes based on a linear reconstruction will be inefficient for well modeling in the general case. In [30], Pedrosa and Aziz presented a logarithmic near-well scheme for the discretization of the flow equations in the well vicinity. Their approach, however, is applicable for isotropic medium and radial grids only. Moreover, it involves a heuristic treatment of grid blocks in the transition between the near-well grid and the surrounding Cartesian grid. A more general framework for near-well modeling using the MPFA O-scheme on flexible grids was proposed by Ding and Jeannin [11,12]. Based on a splitting of the solution into a singular part stemming from the well singularity and a regular part, they introduce near-well models which reduce the numerical error due to the dominating well singularity. This is achieved with the aid of a logarithmic coordinate transformation, rendering the pressure variation linear in the new coordinate system, and hence a linear scheme is applicable.

In this work we will pursue their approach using flexible near-well grids. We construct analytical solutions for 2D single phase near-well flow which is not aligned with a radial inflow pattern. These solutions resemble strongly heterogeneous, possible anisotropic media. We compare different control-volume discretization schemes and radial-type grids for such cases and give their convergence behavior for single phase flow. The objective is to obtain a clearer view on the accuracy of the near-well grids and discretization schemes for large contrast in permeability, and hence, to determine which is the preferable grid and a suitable numerical scheme given certain near-well conditions. The results of the single-well test cases are supported by simulations involving multiple wells and two-phase flow.

2 Control-volume Formulation

We are concerned with numerical simulations of near-well Darcy flow in anisotropic heterogeneous porous media. Let $\Omega \subset \mathbb{R}^2$ be an open bounded domain containing at least one well. For incompressible fluids, the fluid pressure p behaves as the solution of a steady-state elliptic equation,

$$-\nabla \cdot (\boldsymbol{K}(\boldsymbol{x})\nabla p) = 0, \quad \text{for } \boldsymbol{x} \in \Omega, \tag{1}$$

where $\boldsymbol{K}$ is the symmetric positive definite diffusion tensor. The diffusion coefficients are allowed to be discontinuous across internal boundaries. Let Γ_R and Γ_W denote the reservoir boundary and the well bore boundary, respectively. We assign the following boundary conditions:

$$\begin{aligned} p(\boldsymbol{x}) &= p_w, \quad \text{for } \boldsymbol{x} \in \Gamma_{W,D}, \\ p(\boldsymbol{x}) &= p_r, \quad \text{for } \boldsymbol{x} \in \Gamma_{R,D}, \\ -(\boldsymbol{K}(\boldsymbol{x})\nabla p) \cdot \boldsymbol{n} &= g, \quad \text{for } \boldsymbol{x} \in \Gamma_{R,N}. \end{aligned} \tag{2}$$

Here, the vector $\boldsymbol{n}$ is the outward normal on $\Gamma_{R,N}$. The well flow rate Q is given by the relation

$$-\int_{\Gamma_W} (\boldsymbol{K}\nabla p) \cdot \boldsymbol{n}\, d\sigma = Q, \tag{3}$$

with $\boldsymbol{n}$ now being the outward normal on the well bore.

Let $\{\mathcal{T}_h\}$ be a family of partitions of Ω into non-overlapping elements E. In reservoir flow simulation we aim at a consistent reconstruction of the flux

$$f_i = -\int_{S_i} (\boldsymbol{K}\nabla p) \cdot \boldsymbol{n}\, dS, \tag{4}$$

over face S_i of an element. A control-volume formulation of Eq. (1) will in general provide an expression for the face fluxes based on several local pressure values,

$$f_i \approx \sum_{j \in M} t_{i,j} p_j. \tag{5}$$

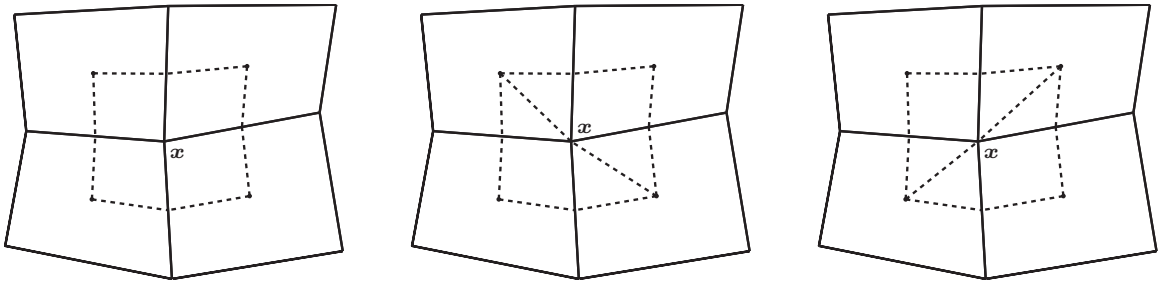

(a) O-shaped coupling. (b) L-shaped coupling. (c) L-shaped coupling.

Fig. 1: Consider four quadrilateral cells with a common node $\boldsymbol{x}$. Bounded by the dashed lines are the interaction volumes for the MPFA O- and L-scheme, respectively. Subface fluxes are computed locally within each interaction volume.

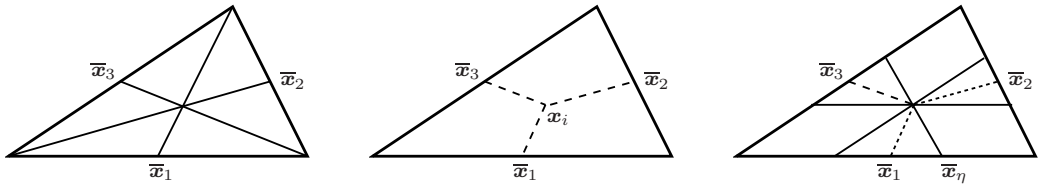

(a) The lines from each vertex to the opposite face midpoint $\overline{\boldsymbol{x}}_i$, respectively, intersect at the barycentre $\boldsymbol{x}_i$.

(b) Each triangle E_i renders three subcells for local flux approximation.

(c) The pressure continuity point $\overline{\boldsymbol{x}}_\eta$, where $\eta = 1/3$.

Fig. 2: The O(1/3)-method for triangular grids.

We denote by $t_{i,j}$ the transmissibility coefficients and by M the set of cells contributing to the flux f_i.

2.1 Multipoint Flux Approximation

Due to its ease of implementation, computational speed and robustness, a two-point approximation (TPFA) of (4) is a widely used numerical scheme in reservoir simulation. Computing the flux f_i then involves the cell center pressure values in the two cells adjacent to face S_i,

$$f_i \approx t_{i,j}\,(p_{j^+} - p_{j^-}). \tag{6}$$

A TPFA scheme yields a consistent flux reconstruction for $\boldsymbol{K}$-orthogonal grids. In the general case of non-orthogonal grids and full tensor anisotropy, however, the two-point scheme does not render a consistent flux approximation [2]. Hence, to amend this deficiency, multipoint flux approximations (MPFA) were introduced, see, e.g., [1,3,4,14,15] and references therein. This class of schemes has proven to be a powerful discretization tool for general grids and discontinuous, anisotropic diffusion coefficients [5,20].

Consider Fig. 1a. The MPFA O(η)-scheme introduces a dual grid for local transmissibility calculations at subfaces. Then, face transmissibilities are found by an assembly of the subface transmissibilities, respectively. Locally, the dual grid constitutes an interaction region. In this local flux reconstruction, the O(η)-scheme assumes full flux continuity over the subfaces in the interaction region and pressure continuity at a point $\overline{\boldsymbol{x}}_\eta$ at each subface. Here, the parameter η is the relative distance from the face midpoint to the continuity point. In this work, we discuss the well-known O(0)-method and the recently proposed O(1/3)-method [17,19]. The latter is introduced for triangular grids, for which it is shown to be symmetric (see Fig. 2) and robust with respect to convergence. We remark that in [17], an example with the O(1/3)-method on a locally refined unstructured grid in the well vicinity is shown. They consider radial flow towards the well, and similar to our approach, the well bore itself is discretized. Other choices for the continuity point $\overline{\boldsymbol{x}}_\eta$ are discussed in, e.g., [14, 15]. Moreover, see, e.g., [9,16,21,32] for other methods that utilize a multipoint flux stencil.

Similarly, the MPFA L-method [6] introduces a dual grid like the O-scheme. However, it seeks to reduce the number of cell entries in the flux stencil with the aid of a selection criterion in the local flux reconstruction. Transmissibility coefficients are found by assuming full continuity of both flux and pressure at the subfaces of

each interaction region. This can be arranged in two ways for each interaction volume, see Figs. 1b-1c.

We note that both the MPFA O(0)- and L-scheme reduce to a two-point scheme when applied to a $\boldsymbol{K}$-orthogonal grid.

3 Near-well Grids

A flexible near-well grid with a radial-like nature is the reasonable choice for accurate near-well simulations. This is in agreement with the nature of the well inflow pattern. Moreover, as the pressure behaves logarithmically rather than linear in the well vicinity, we seek a grid which is adapted to this behavior. This means a logarithmic refinement of the grid.

Also, the impact of the complexity in the near-well region may vary along the well bore. Hence, the grid generation should be independent of possible anisotropies or heterogeneities. We will accomplish this by following the methodology of Ding and Jeannin in [12]. We generate our near-well grids with the aid of a coordinate transformation from Cartesian coordinates to coordinates on logarithmic scale,

$$\begin{aligned} x &= e^{\,\rho}\cos\theta, \\ y &= e^{\,\rho}\sin\theta, \end{aligned} \tag{7}$$

with $\theta \in [0, 2\pi]$ and $\rho \in (-\infty, +\infty)$. We denote by $\mathcal{P}$ the physical space, and by $\mathcal{R}$ the logarithmic reference space. The pressure variation due to the well singularity now has a linear behavior in $\mathcal{R}$. Moreover, the circular well bore boundary transform to a line for which $\rho = \ln r_w$.

The solution still satisfies an elliptic equation in the new coordinate system. Fluxes are also being conserved under the transformation, that is; the flux across a curve in the physical coordinate system equals the flux across the transformed curve in logarithmic space $\mathcal{R}$. Hence,

$$f_i = -\int_{S_i} (\boldsymbol{K}\nabla p)\cdot \boldsymbol{n}\, dS = -\int_{\hat{S}_i} (\hat{\boldsymbol{K}}\nabla p)\cdot \hat{\boldsymbol{n}}\, d\hat{S}, \tag{8}$$

where $\hat{\boldsymbol{n}}$ is an outer normal vector in $\mathcal{R}$, and with $\hat{\boldsymbol{K}}$ being the transformed diffusion tensor,

$$\hat{\boldsymbol{K}} = J\,\boldsymbol{D}^{-1}\boldsymbol{K}\,\boldsymbol{D}^{-T}. \tag{9}$$

Here, $\boldsymbol{D}$ is the Jacobian matrix of the transformation,

$$\boldsymbol{D} = e^{\,\rho}\begin{pmatrix} \cos\theta & -\sin\theta \\ \sin\theta & \cos\theta \end{pmatrix}, \tag{10}$$

and the determinant J is given as $J = e^{2\rho}$.

Consider Fig. 3a and Fig. 3b. A rectangular grid in the logarithmic reference system is the equivalence of a radial grid in the coordinate system $\mathcal{P}$, while a triangular grid in the logarithmic space becomes an unstructured curved grid in the physical space under the transformation. Thus, when discretizing in $\mathcal{R}$, we utilize grid blocks in the logarithmic space for which edges are non-curved. We employ a triangular grid consisting of isosceles triangles.

Furthermore, we may discretize on the physical grid blocks directly, see Fig. 4. These grids are conceptually similar to the grids in Fig. 3a and Fig. 3b. However, each curved face is replaced by its respective line segment. Finally, observe that the well bore is approximated by a polygon for the physical space grids.

4 Single Phase Simulations

In this section, we present the convergence behavior of the MPFA O- and L-scheme for some complex near-well flow regimes. The investigations here are limited to single phase flow. We apply logarithmic radial and triangular grids. The errors are measured in discrete L^2 norms for the pressure and the normal velocities. We denote by the subscript h, the discrete values. Let A_E be the area of a grid cell $E \in \mathcal{T}_h$. Then, for the pressure, we define

$$\|p - p_h\|_{(L^2,h)} = \left(\frac{\sum_{E\in\mathcal{T}_h} A_E (p_E - p_{h,E})^2}{\sum_{E\in\mathcal{T}_h} A_E}\right)^{1/2}.$$

We denote by $\mathcal{E}_k$, the set of all element faces in $\mathcal{T}_h$. Let W_e be the area associated to a face $e \in \mathcal{E}_k$. Here, $W_e = \frac{1}{C_{\mathcal{T}_h}}(A_{E_1} + A_{E_2})$, where A_{E_i}, $i = 1, 2$, is the area of the cell E_i adjacent to face e. The constant $C_{\mathcal{T}_h}$ relates to the number of faces for each element. Thus, for the radial grid, $C_{\mathcal{T}_h} = 4$, and for the triangular grid, $C_{\mathcal{T}_h} = 3$. Then, the discrete L^2 norm for the normal velocities are given by

$$\|u - u_h\|_{(L^2,h)} = \left(\frac{\sum_{e\in\mathcal{E}_k} W_e((u_e - u_{h,e})/|e_h|)^2}{\sum_{e\in\mathcal{E}_k} W_e}\right)^{1/2},$$

where u_e is the normal velocity across the edge e. We also provide the results measured in discrete maximum norm.

4.1 Anisotropy

The first test involves a homogeneous, but anisotropic medium. A thorough investigation by Peaceman in [27], showed that the true near-well flow pattern in the case of an anisotropic permeability has an elliptic nature.

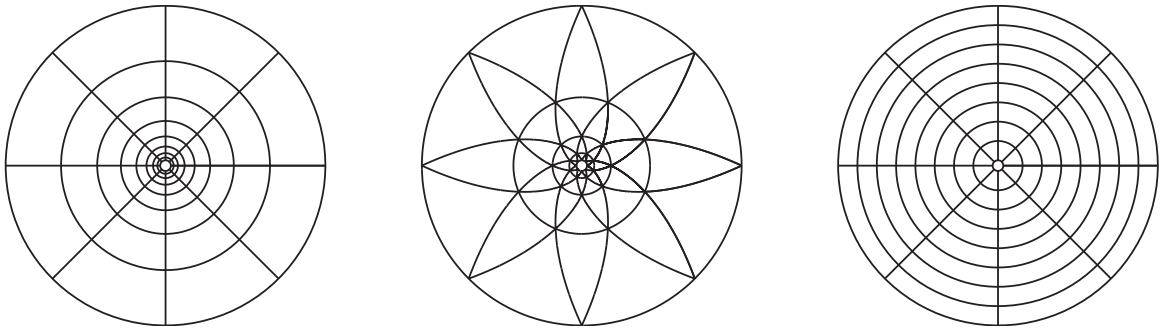

(a) Logarithmic radial grid. (b) Logarithmic triangular grid. (c) Equidistant radial grid.

Fig. 3: Grids adapted to the flow behavior of the near-well region. Figure 3a and 3b show near-well grids with logarithmic refinement. These grids have their equivalent grids in a logarithmic reference space. In Figure 3c, the grid is equidistant.

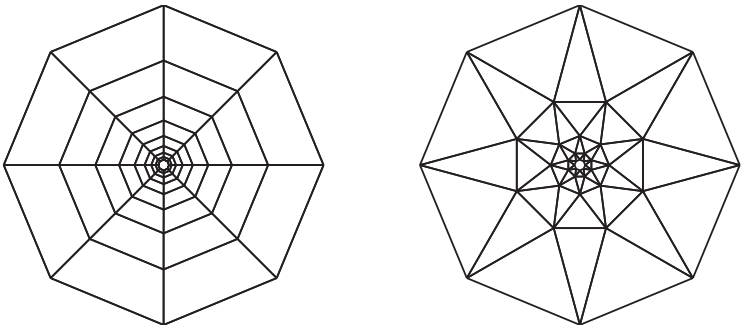

(a) Radial near-well grid. (b) Triangular near-well grid.

Fig. 4: Grids adapted to the logarithmic flow behavior of the near-well region.

Denote by k_x and k_y the permeability in the x- and y- direction, respectively. Assume $k_x > k_y$. Let

$$\begin{aligned} x &= (k_x/k_y)^{1/4} b \sinh\rho \sin\theta, \\ y &= (k_y/k_x)^{1/4} b \cosh\rho \cos\theta. \end{aligned} \tag{11}$$

Here, the constant b depends on the well bore radius r_w and the permeability,

$$b^2 = \frac{r_w^2(k_x - k_y)}{\sqrt{k_x k_y}}. \tag{12}$$

The exact anisotropic solution to Eq. (1) is computed with the aid of the elliptical (ρ, θ)-coordinates,

$$p = p_w + \frac{Q}{2\pi(k_x k_y)^{1/2}}(\rho - \rho_w), \tag{13}$$

where $\tanh^2\rho_w = k_y/k_x$ is the parameter identifying the well bore.

Contrary to the isotropic case, for which the pressure contours are circular and streamlines are purely radial, Peaceman found that the isobars in the anisotropic case rapidly turn into ellipses away from the circular well bore. Furthermore, the streamlines will follow a hyperbolic trajectory, see Fig. 5. This observation implies that, in the case of an anisotropic permeability, a radial grid will not be aligned with the true flow behavior. We will have flow across the radial beams of the grid. Our aim is yet to investigate whether such a radial or a triangular grid, along with a suitable discretization scheme, yield an accurate prediction of the near-well flow with anisotropic diffusion coefficients. We also compare the convergence behavior of discretization in physical space $\mathcal{P}$ and the logarithmic reference space $\mathcal{R}$. Finally, we assign Dirichlet boundary conditions both on the well bore boundary and the exterior boundary.

However, how far from the well bore the singular flow should be accounted for is a question not fully resolved. Albeit our focus is a model for accurate prediction of the well inflow, we should also keep in mind that the near-well grid needs to match a surrounding grid. A reservoir grid block will in general be on the scale of tens of meters, which is considerably larger than the well

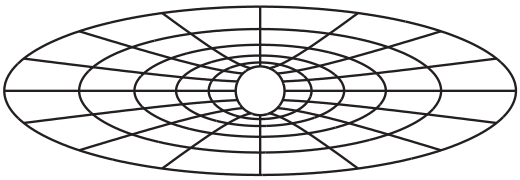

Fig. 5: Near-well flow pattern for the anisotropic, homogeneous case. Isocontours are ellipses with increasing eccentricity and streamlines are hyperbolas. Here $\kappa = 10$.

bore diameter. Thus, we have chosen the outer radius r_e of the near-well region to be of the size $r_e = 100 \times r_w$.

The numerical convergence behavior for the logarithmic grids in Fig. 3a, Fig. 3b and Fig. 4 is seen in Fig. 6 - 11. Firstly, we observe that the TPFA scheme does not converge, neither for discretization in the space $\mathcal{P}$ nor the space $\mathcal{R}$. See Fig. 6 and Fig. 9, where the scheme is applied to the radial grid with anisotropy ratio $\kappa = 5$. The result is as expected since the radial grid, when imposing an anisotropic permeability, is no longer $\boldsymbol{K}$-orthogonal in either of the discretization spaces.

For the MPFA simulations, we have employed anisotropy ratios κ of 5 and 20. Consider the error measured in discrete L^2 norm. Given $\kappa = 5$, we observe h^2-convergence for the pressure on both radial and triangular grids. This applies to discretization in reference space as well as in physical space. The same convergence rate is seen also for the normal velocity. However, for the triangular $\mathcal{R}$-space discretization, we find a slight degradation in the convergence order. Let $\kappa = 20$. We find here a convergence behavior similar to the previous case for the radial grid. The pressure convergence is still h^2 in both the $\mathcal{P}$ and $\mathcal{R}$ space for the triangular grid. Now, the normal velocity is seen to converge slightly slower in both spaces for this grid. We may, however, expect the asymptotic rate of convergence to reach 2 for both values of κ.

Moreover, considering the error bounds itself, we find that the triangular grid performs significantly better than the radial grid. This applies to both anisotropy ratios and discretization spaces. Note that, also MPFA schemes with other values of the parameter η have been tested for the local triangular grid. They are seen to yield error bounds lying between the error bounds for the radial grid and the triangular grid utilizing the O(0)- and O(1/3)-method, respectively. Thus, the O(1/3)-scheme seems to be the optimal choice.

In discrete L^∞ norm, the pressure is seen to converge very close to h^2 for all cases. For the normal velocity, the results are more spread out. The convergence lies between h^1 and h^2. Finally, when measured in maximum norm, the difference in the error bounds for the two grids is no longer as significant as in discrete L^2 norm.

Now, discussions in the literature, see, e.g., [12], suggest that a linear approach in the well vicinity is inefficient if the near-well grid blocks are of size larger than the well bore itself. A linear grid, that is; a uniform grid in radial direction, is seen in Fig. 3c. Numerical tests, similar to the anisotropic near-well flow described above, support this. Consider Fig. 12. We define a parameter $\beta \in [0, 1]$, to describe the degree of logarithmic refinement of the near-well grids. Denote by γ_r a grid line in the near-well grid for which the radius r is constant and $\theta \in [0, 2\pi]$. Further, let $\gamma_{r,\log}$ and $\gamma_{r,\text{lin}}$ denote the corresponding grid line for a logarithmic near-well grid and a linear near-well grid, respectively. Then, we obtain grids with varying degree of logarithmic refinement by the relation

$$\gamma_r = \beta\gamma_{r,\log} + (1 - \beta)\gamma_{r,\text{lin}}. \tag{14}$$

When $\beta = 0$, the grid is linear, and $\beta = 1$ yields the logarithmic grid. We observe that as $\beta \to 1$, the convergence properties are improved, however, we do not obtain full h^2-convergence until the grid is fully logarithmic. These observations apply to the triangular grid as well. However, note that as $r_e \to r_w$, the difference between a linear and logarithmic refinement becomes less significant. With a near-well region defined within only a few well radii for instance, the linear approach seems to work as well as the logarithmic approach.

Finally, when applied to the local triangular grid, we note that the L-scheme behaves poorly. For an anisotropy ratio $\kappa = 5$, only the pressure measured in discrete L^2-norm, exercises h^2-convergence. The normal velocity converges with reduced rates in both norms. For both variables the errors are significantly larger than for the O(1/3)-method. For stronger anisotropies, however, we meet some computational challenges with the scheme. The system matrix becomes ill conditioned as the grid is refined, and this applies to discretization in both $\mathcal{P}$- and $\mathcal{R}$-space. This is a topic for further investigations, however, we note that the L-scheme originally was constructed for quadrilateral grids. Numerical tests for regular triangular grids can be found in [23], where the method is seen to work well for general anisotropic and heterogeneous problems. However, in [18], the L-scheme is found to perform poorly also for distorted triangular meshes.

4.2 Heterogeneous Isotropic Medium

Next, we aim at investigating the numerical convergence behavior in the case of a heterogeneity in the

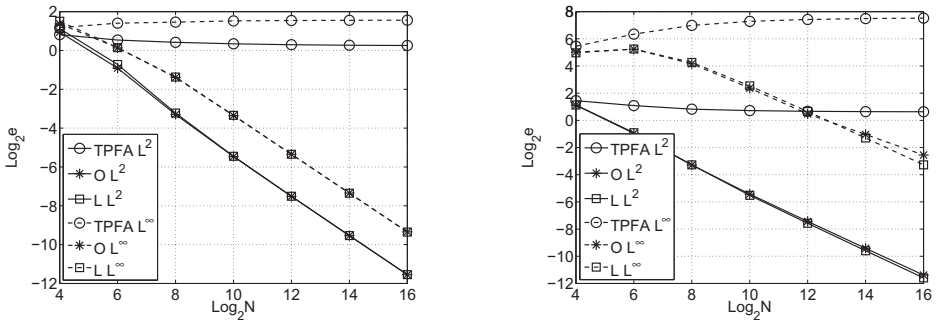

(a) Potential (b) Edge normal velocity

Fig. 6: Solution 13. Anisotropy ratio 5. Radial grid with discretization in logarithmic space. N is the number of grid cells.

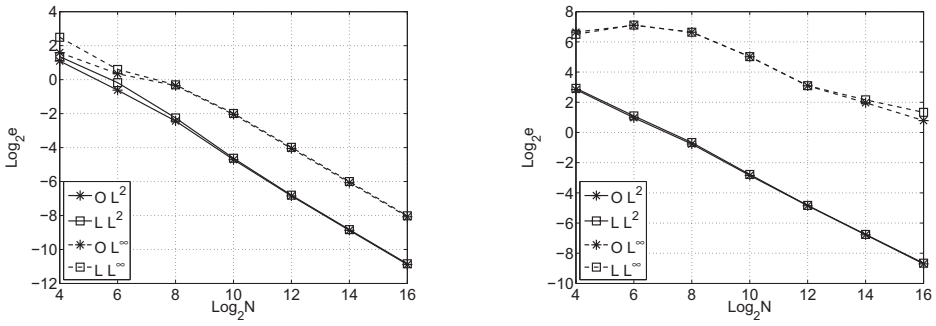

(a) Potential (b) Edge normal velocity

Fig. 7: Solution 13. Anisotropy ratio 20. Radial grid with discretization in logarithmic space. N is the number of grid cells.

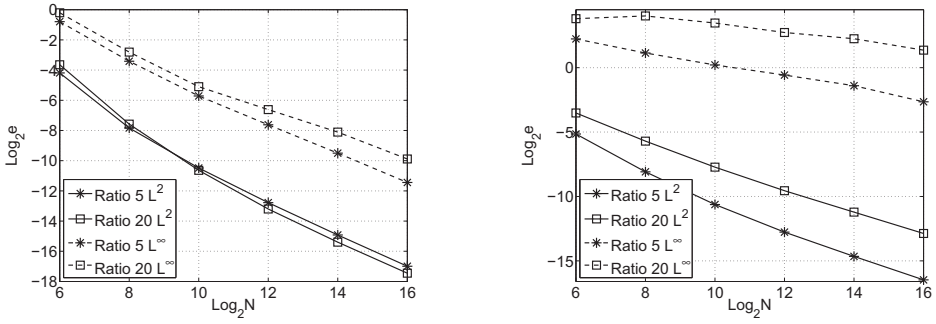

(a) Potential (b) Edge normal velocity

Fig. 8: Solution 13. Anisotropy ratios 5 and 20. Triangular grid with discretization in logarithmic space. N is the number of grid cells.

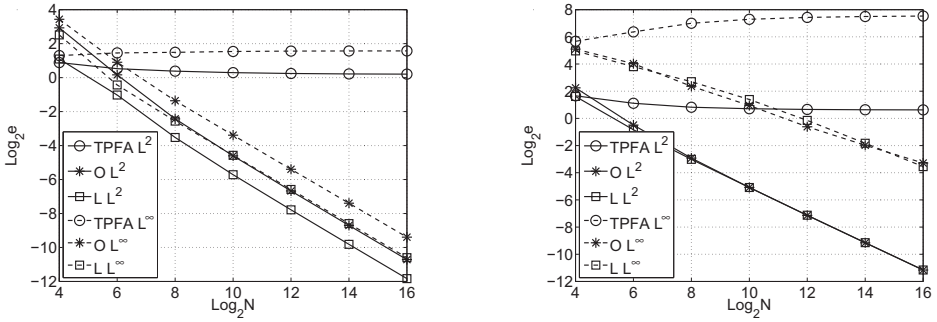

(a) Potential (b) Edge normal velocity

Fig. 9: Solution 13. Anisotropy ratio 5. Radial grid with discretization in physical space. N is the number of grid cells.

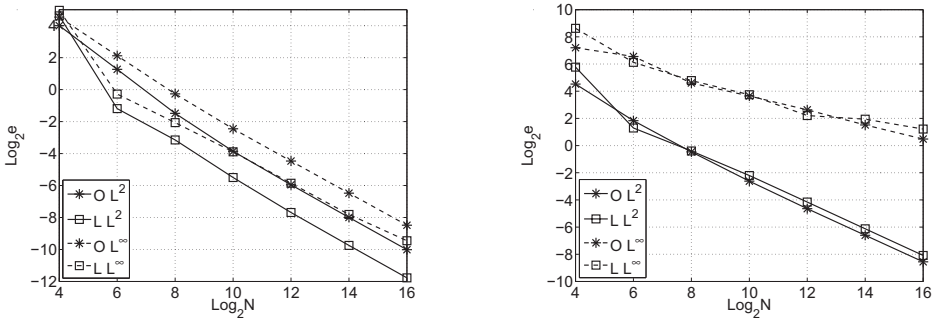

(a) Potential (b) Edge normal velocity

Fig. 10: Solution 13. Anisotropy ratio 20. Radial grid with discretization in physical space. N is the number of grid cells.

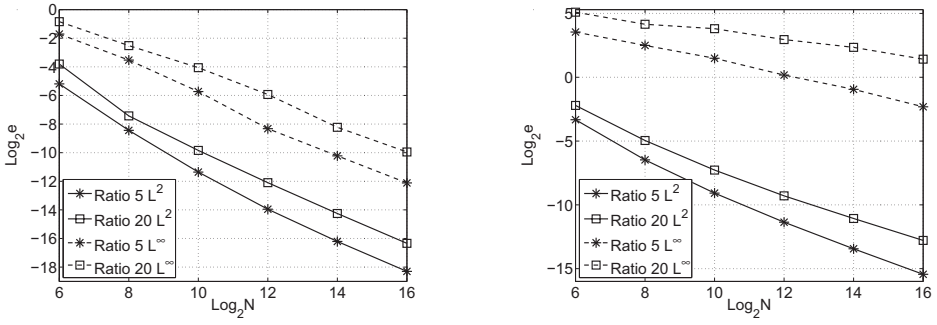

(a) Potential (b) Edge normal velocity

Fig. 11: Solution 13. Anisotropy ratios 5 and 20. Triangular grid with discretization in physical space. N is the number of grid cells.

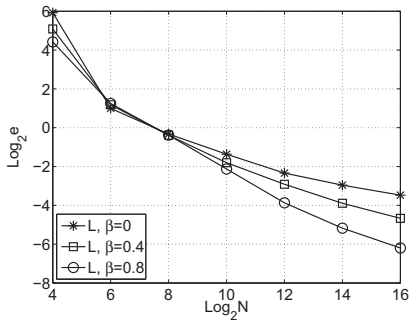

Fig. 12: Discrete L^2 error of normal velocity. The parameter $\beta \in [0, 1]$ describes the degree of logarithmic refinement of the grid. For $\beta = 0$, the grid is linear. We observe that as $\beta \to 0$, the converge rate deteriorates. For $\beta = 0$, the converge rate is 0.6 in the last refinement step.

near-well region. By imposing a barrier in the well vicinity, we find a violation of the radial inflow pattern towards the well. This may also resemble a multiphase flow simulation, where the phases obstruct the flow of each other.

We seek, in the physical space, an obstacle which is aligned with the shape of the radial grid blocks as seen in Fig. 3a. A semi-analytical solution for this case may be constructed with the aid of the Schwarz-Christoffel mapping to some polygonal region, on which we may solve our boundary value problem. The algorithm may be described as follows.

Consider a domain with the well bore centered at the origin. Denote by $z = re^{i\theta}$ a point in this physical domain. We enforce a barrier which is symmetric about $\theta = 0$. Thus, by exploiting the angular symmetry, we may regard the upper half of the grid only. This is visualized in Fig. 13a. Under the transformation

$$z = e^w, \tag{15}$$

this domain is the image of the polygonal domain seen in Fig. 13b. The points z_j, $j = 1, \ldots, 8$, define the geometry of the physical problem and correspond to the corners w_j, $j = 1, \ldots, 8$, of the polygon, respectively. The outer radius of the domain is set according to $z_6 = 30 \times z_1$. Now, we impose uniform Dirichlet conditions on the polygon boundaries w_1w_8 and w_6w_7, corresponding to the well bore boundary and the outer boundary, respectively. The boundaries w_jw_{j+1}, $j = 1, \ldots, 5, 7$, are no-flow boundaries. These boundary conditions are preserved under the conformal map (15).

We will now exploit the properties of the Schwarz-Christoffel (SC) map to obtain a semi-analytical heterogeneous solution on the polygon. Let $\pi\alpha_j$, $j = 1, \ldots, 8$, denote the interior angles at the polygon vertices. Then, the explicit SC formula from the unit disk to the polygon reads

$$f(\eta) = f(0) + C \int_0^\eta \prod_j^8 (s - \eta_j)^{\alpha_j - 1}\, dS. \tag{16}$$

Here, C is a complex constant and η_j are prevertices of the polygon vertices w_j, $j = 1, \ldots, 8$, respectively. The solution procedure involves computing $f^{-1}(\eta)$ from the polygon to the disk, and further, a forward SC map to a representative polygonal region taking the boundary conditions into account. Finally, the solution is extracted. In the computation we employ the Schwarz-Christoffel Toolbox for MATLAB developed by T. Driscoll. See [13] for documentation. In Fig. 13c, the isobars and streamlines of the solution are visualized on the whole physical domain.

We simulate on both near-well grids. The curved shape of the barrier necessitates a reference space discretization. Note that for the radial grid, the mesh in the space $\mathcal{R}$ is $\boldsymbol{K}$-orthogonal. Hence, the MPFA O(0)-scheme reduces to the TPFA scheme for this simulation. We note, however, that for the triangular grid, the full O(1/3)-stencil still applies.

The heterogeneity constitutes an exterior angle $\beta = 3\pi/2$ to the surrounding medium. Let $\alpha = \pi/\beta = 2/3$. According to finite element theory [6,33], we expect a convergence order in discrete L^2 norm of $h^{2\alpha}$ for the pressure and h^α for the normal velocity. The numerical convergence is seen in Fig. 14. We find both grids to meet the expected convergence rates, and again, the triangular grid yields a smaller error than the radial grid. Measured in discrete maximum norm, the observed convergence is h^α for the pressure. The normal velocity is not seen to converge. This applies to both near-well grids. These results are in agreement with the discussion in [5].

4.3 Multiple Wells

In Section 4.1, we provided quadratic convergence for the near-well models in an anisotropic yet homogeneous medium for single well cases. Here, we impose a flow regime involving several wells in an anisotropic reservoir. Thus, we must account for the transition between the near-well regions and the reservoir region in the simulations henceforth. That is; we need to connect the flexible near-well grid with a surrounding global grid.

Consider Fig. 15. We impose one injector I and two producers, P_1 and P_2, to be located on two impermeable boundaries of the domain, respectively. The medium

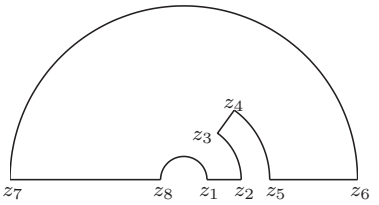

(a) The points z_j, $j = 2, \ldots, 5$, define the barrier. The well bore is delineated by z_1 and z_8.

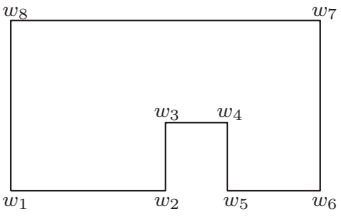

(b) Preimage of the physical domain.

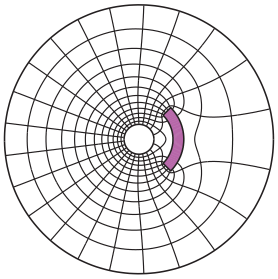

(c) Isobars and streamlines for the semi-analytical heterogeneous solution.

Fig. 13: We obtain a polygonal shape of our domain via the mapping $z = e^w$. Note that, for visualization purposes, the scaling is not correct. The solution for the full domain is seen to the right.

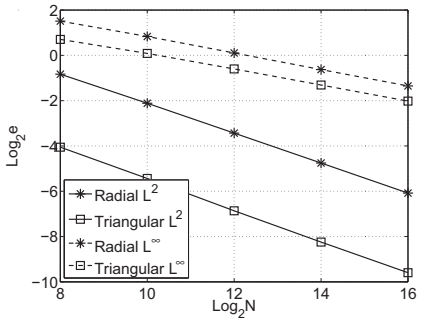

(a) Potential

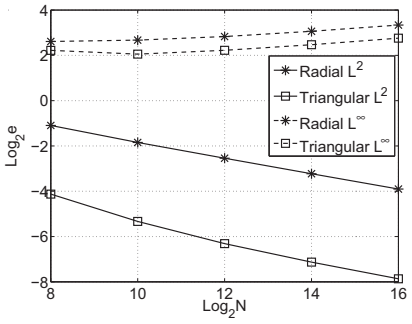

(b) Edge normal velocity

Fig. 14: Near-well heterogeneity. Radial and triangular grids with $\mathcal{R}$-space discretization. N is the number of grid cells.

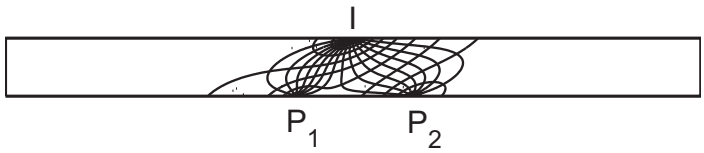

Fig. 15: Pressure contours and streamlines for the flow from an injector I towards the producers P_1 and P_2 for the point sink/source approach. The angles in the triangle IP_1P_2 at P_i, $i = 1, 2$, are 45^o.

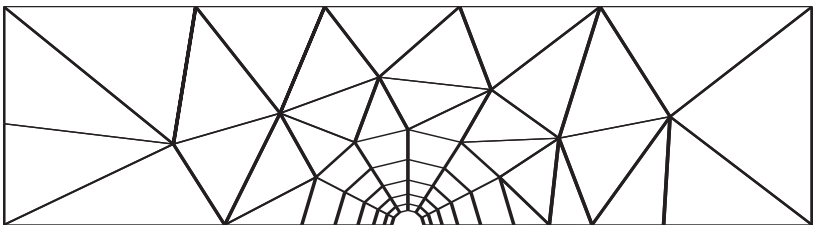

Fig. 16: Transition between a radial near-well grid and a triangular grid in the reservoir. Note that, for visualization purposes, this is not a snap-out of the grid we use for simulation.

anisotropy ratio κ is set to 5.8, and the principal direction associated with the larger eigenvalue is rotated with an angle $\phi = 22.5^{\text{o}}$ from the horizontal axis. An analytical solution to such a problem using a point sink/source well approach is found in example 2 in [2]. Our near-well approach, however, takes a finite well bore radius into account. Motivated by [27,28], we assign uniform Neumann boundary conditions on the well bore boundaries.

According to the point sink/source solution, the flow pattern is radial in the vicinity of the wells, whereas for a finite well bore, we have seen that the streamlines have a hyperbolic character. However, according to the discussion by Peaceman in [29], this difference decreases rapidly as we move away from the well bore. Thus, despite the differences in the two problems, the point sink/source solution resembles the actual problem we simulate quite well. We cannot, though, expect the numerical solution to converge to the point sink/source solution.

The outer radius r_e of each near-well region is here set to $r_e = 10 \times r_w$, with r_w being the well radius. The height h between the two impermeable boundaries we define to be $h = 100 \times r_w$. In the near-well regions, we will apply both the triangular and radial grid. Furthermore, the near-well regions are joined by a surrounding triangular grid. This grid is generated by an algorithm of Persson and Strang [31], with some minor modifications to avoid hanging nodes in the transition zone between the meshes. In Fig. 16, the coupling of a radial near-well grid and a circumjacent triangular grid is visualized. Note that in a full-scale simulation, the triangular grid in Fig. 16 may also play the role of an intermediate grid between the near-well grid and a global rectangular grid.

For the triangular grid we will still use the O(1/3)-method, while we apply the O(0)-method only for the radial grid. We measure the difference between the numerical solution and the point sink/source solution in the discrete L^2 norm.

The findings in Section 4.1 showed a rather small discrepancy between discretization in $\mathcal{R}$ and discretization in $\mathcal{P}$. The same tendency is observed here, and this applies to both meshes. Yet, due to the disparity of the two problems here, we cannot test for convergence of the models. Contrary to the results of Section 4.1, we have no means to establish which discretization space yields the more reliable results. However, due to ease of implementation, and possible complications in combining two different discretization spaces, we suggest to apply a physical space discretization in this case. In addition, following the discussion in [8], combining two different MPFA methods may yield less accurate results. Here, we combine the O(0)- and O(1/3)-method in the case of a radial near-well grid. Also, for near-well discretization in $\mathcal{R}$, we combine a logarithmic MPFA near-well scheme with a linear MPFA scheme. And again, due to the lack of a proper analytical solution, we cannot conclude on this issue.

Hence, with discretization in $\mathcal{P}$, and for a grid with 948 cells, of which 32 is located in each of the near-well regions, respectively, the difference in the pressure is 1.2×10^{-2}, while the difference in the flux is 2.7×10^{-3}. This applies to both near-well grids. Further refinements do not yield a smaller error. Finally, a closer look at the solutions (not shown here) indicates no difficulty in the transition between the logarithmic and linear grids.

5 Multiphase Simulations

In the previous section, we studied the numerical behavior of some control-volume MPFA schemes on flexible near-well grids for single phase flow. Also, we presented a way to couple the near-well grids with a surrounding global grid.

When coupled to a transport equation, analysis of the pressure equation becomes more involved. Thus, in the literature, analysis of MPFA methods is done by considering flow of a single phase only. Hence, for multiphase analysis, we resort to numerical experiments.

In this section, we extend the near-well models to treat multiphase flow. We study, and compare, the discretization schemes and the near-well grids for a simple two-phase simulation. The well is horizontal, pointing in the y-direction, and the simulations are performed in an xz cross section. The main purpose of this exercise is to examine the applicability of our well models to simulations of multiphase flow.

5.1 Experimental Setup

The flow is described by the conservation equations

$$\phi\rho_\alpha \frac{\partial S_\alpha}{\partial t} - \nabla \cdot (\rho_\alpha \boldsymbol{u}_\alpha) = q_\alpha, \tag{17}$$

for each phase $\alpha = w, o$. Denote by subscript w the wetting phase (water) and o the non-wetting phase (oil). Let ϕ be the porosity, S_α the phase saturation and let q_α be the source terms. The phase densities ρ_α are set according to $\rho_o/\rho_w = 0.8$. Capillary forces and compressibility are neglected. The Darcy velocity $\boldsymbol{u}_\alpha$ for each phase reads

$$\boldsymbol{u}_\alpha = -\lambda_\alpha \boldsymbol{K}(\nabla p - \rho_\alpha g \nabla z), \qquad \alpha = w, o, \tag{18}$$

where $g\nabla z$ is the gravity term, and λ_α are the phase mobilities. Now, p denotes the flow potential. We employ quadratic relative permeabilities. The permeability $\boldsymbol{K}$ is assumed to be homogeneous, yet anisotropic. The anisotropy ratio is set to $k_x/k_z = 2$, hence, none of the near-well grids are $\boldsymbol{K}$-orthogonal for these simulations. Residual saturations for both phases are set to zero. Finally, the viscosities μ_α are set to be constant, with $\mu_o/\mu_w = 5$.

The equations are solved in an IMPES formulation [10], and the saturations are propagated through the medium by employing a single-point upwinding scheme [7].

For the sake of simplicity, all simulations are carried out for a single production well. We confine the near-well region within $r_e = 30 \times r_w$ in radial direction. Both the triangular and radial near-well grid will be studied, and we employ, for discretization of the pressure equation, the O(1/3)- and O(0)-scheme, respectively. Again, the near-well grids are coupled to a triangular global grid as described in Section 4.3. The outermost cells in the local near-well grids and the neighboring cells in the global grid are of comparable size. Note that, as in Section 4.3, the face transmissibilities in the transition zone between the logarithmic radial grid and the linear triangular grid, will be calculated by a combination of two MPFA methods. And again, near-well discretization in $\mathcal{R}$ implies a combination of a logarithmic MPFA scheme with a linear MPFA scheme.

The initial contact between the water phase and the oil phase is located 50 well radii below the well center. The computational domain is rectangular, and it is large enough to avoid significant influence of the outer reservoir boundaries. On the well bore, a uniform Neumann condition is assigned. For the horizontal reservoir boundaries, we impose a no-flow condition, while on the vertical boundaries, the potential is set to equal the hydrostatic pressure. The saturations are fixed according to the initial contact.

Remark that all figures shown in the following, are zoomed in on the vicinity of the well. Thus, they display a part of the computational domain only.

5.2 Discretization in Physical and Reference Space

As the well starts producing, the water phase will move in upward direction towards the well. Gradually, the saturation profile will cone, and eventually, there will be a water breakthrough. The water phase will subsequently occupy a larger part of the near-well region. This development is shown in Fig. 17 and Fig. 18, for near-well discretization on the logarithmic triangular grid in physical and reference space, respectively.

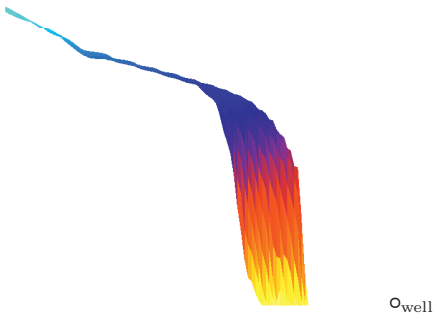

Fig. 19: Local triangular grid. Saturation profile along the vertical line extending through the well bore for the propagation front seen in Fig. 17d. In the grid transition zone, there is a kink in the saturation.

The two time series shown both start at the same point in time, and the data for the subsequent plots are collected at the same time step for both simulations. From the figures, the saturation profiles appear to be equal. A more careful investigation, however, reveals a spatial difference in saturation values of order 10^{-3}. These observations apply to the local radial grid as well (not shown here).

Moreover, from the figures there seems to be a steep saturation gradient in the transition between the local near-well grid and the global grid. This is especially apparent in Fig. 17c and 17d, and Fig. 18c and 18d. Fig. 19 is the saturation profile of Fig. 17d along the vertical line that extends through the well bore. The profile is seen to have a weak kink near the transition zone. This apparent kink in the saturation is probably due to the difference in coarseness between the global grid and the near-well grid, along with the increase in sparsity and degree of unstructuredness of data points in the transition to the global grid. The outer grid cannot represent the flow pattern as accurately as the fine near-well grid. By varying the coarseness of the grids in the simulation, we also observe that as the grids are refined, the apparent kink becomes weaker. Moreover, we have simulated with different choices of r_e (not shown here). From these experiments, we conclude that there will be some weak irregularities in the saturation plots in the transition zones provided that the well has sufficient impact on the dynamics in the transition zone, i.e., the near-well grid does not extend much further than the well's domain of influence.

Even though the saturation profiles resulting from discretization in $\mathcal{P}$ and $\mathcal{R}$ are very similar, they can-

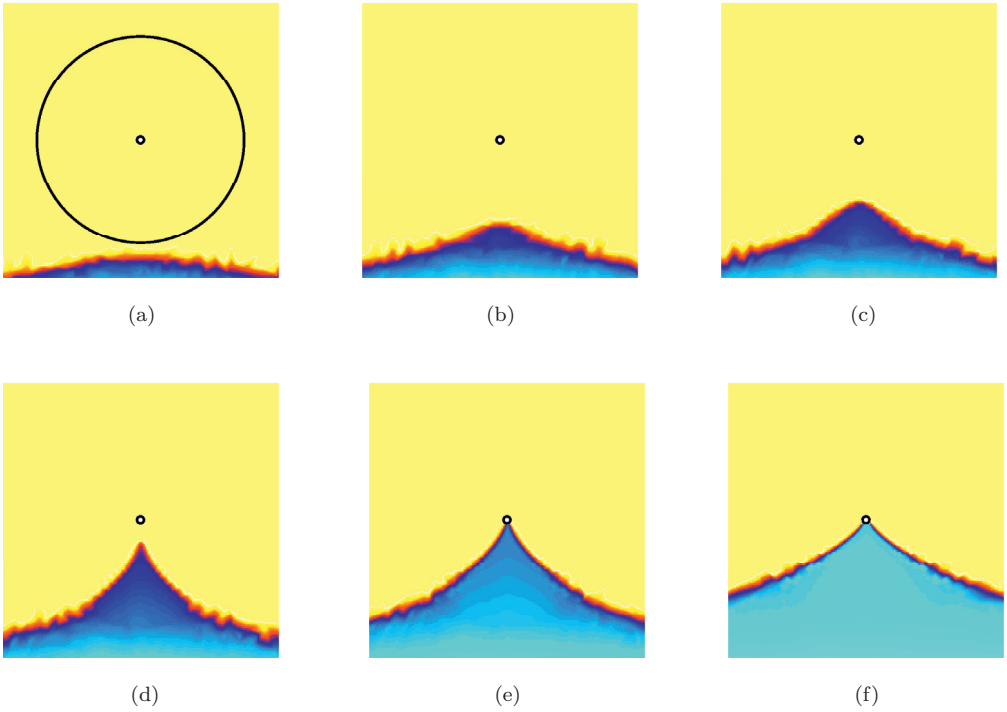

Fig. 17: Physical space discretization: Propagation of near-well saturation fronts. The local grid is triangular and transmissibilities are computed in physical space. The well bore and the outer near-well radius, $r_e = 30 \times r_w$, are shown.

not be considered equal. Like in Section 4.3, we have no means to establish which discretization space provides the more accurate result. However, the disparity of the saturation profiles seen in Fig. 17 and Fig. 18, is much less than the difference in saturation profiles resulting from applying different near-well grids. This will be shown below. Thus, henceforth we compare the near-well grids for different refinement levels, rather than the choice of discretization space. We follow the reasoning of Section 4.3, and choose to apply a physical space discretization from this point on.

5.3 Radial and Triangular Near-well Grid

Here, we compare the local radial and triangular grid. The saturation profiles from the two simulations are qualitatively similar. Prior to the coning of the water phase, the propagation speeds predicted of the two, are very much the same. However, as the saturation fronts enter the near-well region, the local triangular grid predicts a somewhat faster propagation, and hence, an earlier water breakthrough.

The saturation profiles for the breakthrough process are seen in Fig. 20a - 20c and Fig. 20d - 20f, for the triangular and radial grid, respectively. The snap-outs are taken at the same time step for both series. The lack of an analytical solution for this problem, again leaves us unable to conclude on the more reliable of the two simulations.

We note that, when constructing the global grid, the parameters of the gridding algorithm [31], are tuned to get a smooth connection to the near-well grid. This optimization leads to about 25% more cells in the outer global grid for the radial near-well grid than for the triangular. We emphasize that in the local near-well region, there is an equal number of cells.

5.4 Near-well Grid Refinement

The experiments presented in Section 5.2 and 5.3, were all carried out with near-well grids of 4096 (2^{12}) cells. There, we aimed at evaluating different discretization techniques for the near-well flow equations. However, with full-field simulations in mind, it is appropriate to investigate the accuracy of computationally cheaper simulations.

Consider Fig. 21. This figure shows the water propagation for three refinement levels of the triangular near-

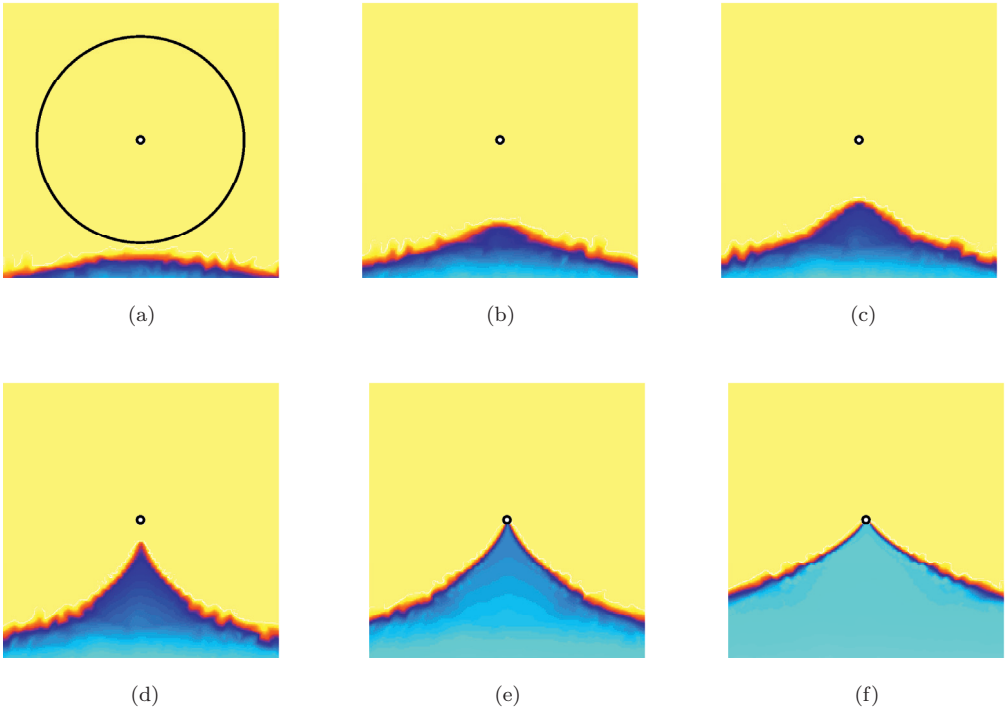

(a) (b) (c)

(d) (e) (f)

Fig. 18: Reference space discretization: Propagation of near-well saturation fronts. Transmissibilities are computed in reference space, and the local grid is triangular. The well bore and the outer near-well radius, $r_e = 30 \times r_w$, are shown.

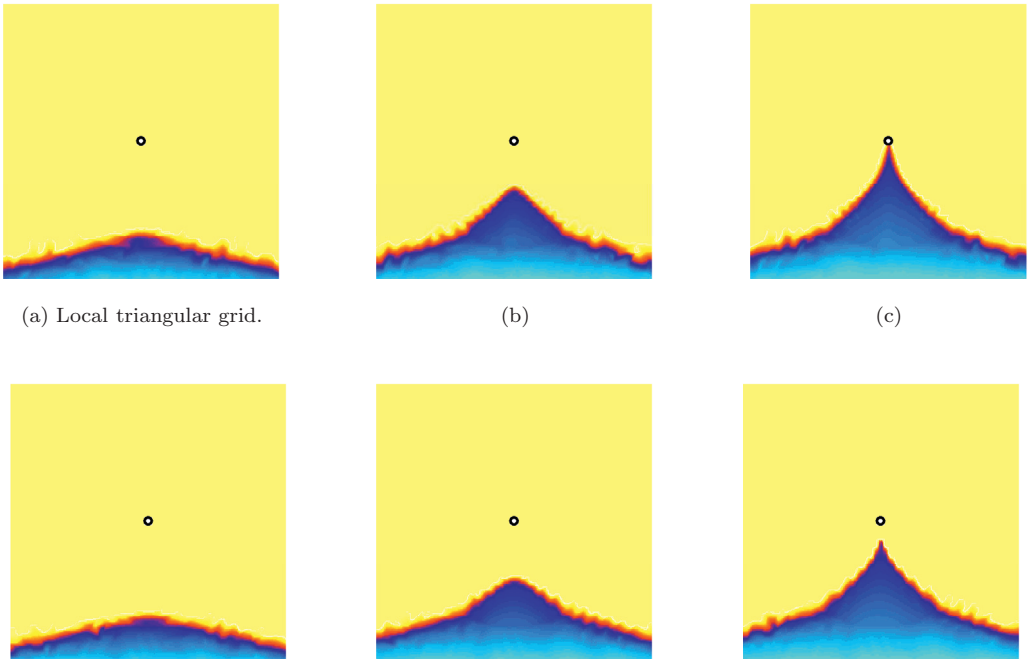

(a) Local triangular grid. (b) (c)

(d) Local radial grid. (e) (f)

Fig. 20: Propagation of near-well saturation front. The local grid is triangular in (a)-(c), while radial in (d)-(f). The triangular grid exhibits an earlier water breakthrough.

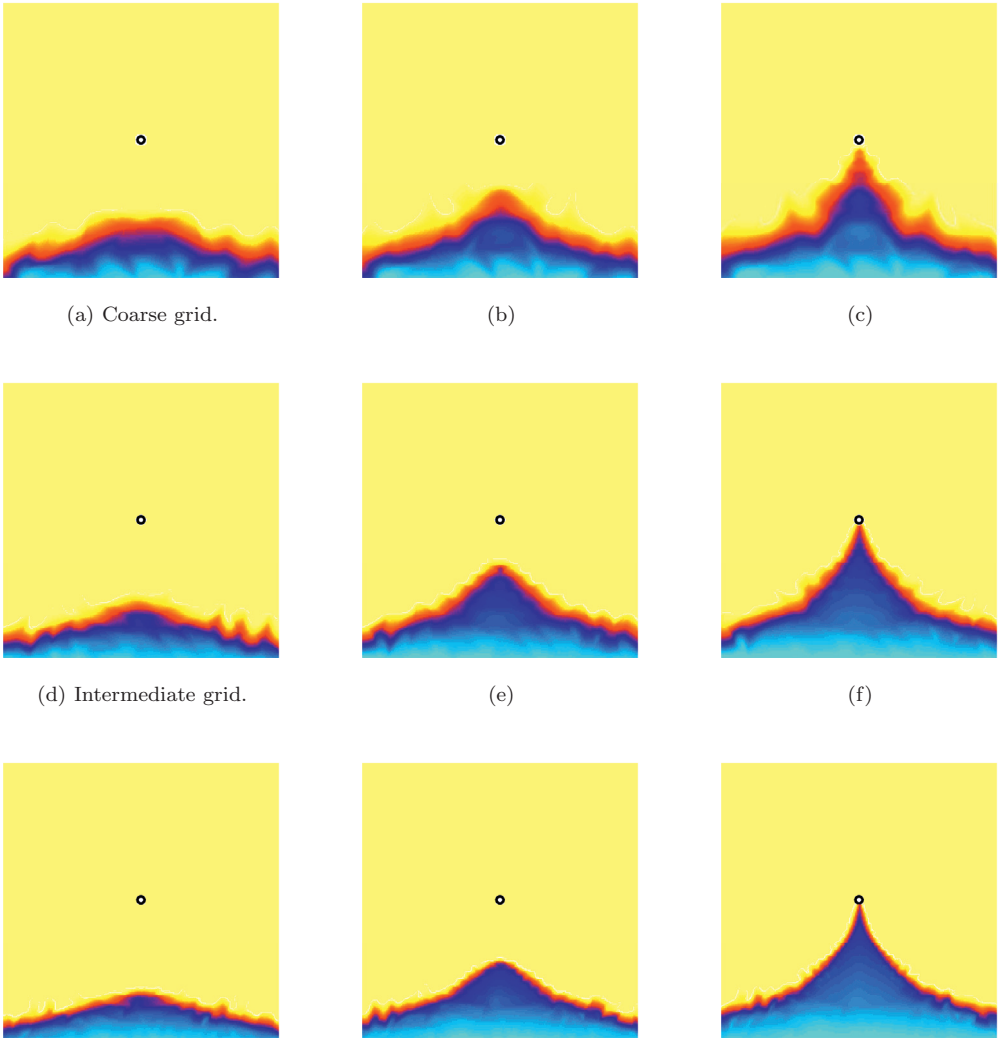

(a) Coarse grid. (b) (c)

(d) Intermediate grid. (e) (f)

(g) Fine grid. (h) (i)

Fig. 21: Propagation of near-well saturation front for three refinement levels of the local triangular grid. The coarse grid in (a)-(c) the front is smeared out. The finer grids in (d)-(f) and (g)-(h) resolve the front well.

well grid at three time levels of the simulations. The series of grids has 2^8, 2^{10} and 2^{12} near-well cells, respectively. The fine grid is the grid employed in the previous simulations.

Clearly, the saturation front is best resolved for the finest grid. However, also the intermediate refinement level yields a fairly good resolution of the front. For the coarse grid, the saturation profile is smeared out, and, by a closer look, one finds the profile to follow the grid lines. Thus, due to the smearing, it is more difficult to localize the front exactly. Again, we emphasize that we cannot conclude on which level yields a certain accuracy.

5.5 Production Data

In Fig. 22, the water cuts are shown for the triangular and the radial near-well grids, respectively. For the triangular grids, the water cuts correspond to the simulations described in Section 5.4. For the local radial grid, the coarse and intermediate grids have the same number of near-well cells as the corresponding triangular grids. The fine radial grid is similar to the grid applied for the simulations seen in Fig. 20d-20f. Moreover, we have applied both a physical and a reference discretization for the fine grids.

First, we note that curves corresponding to discretization in reference and physical space, respectively, are

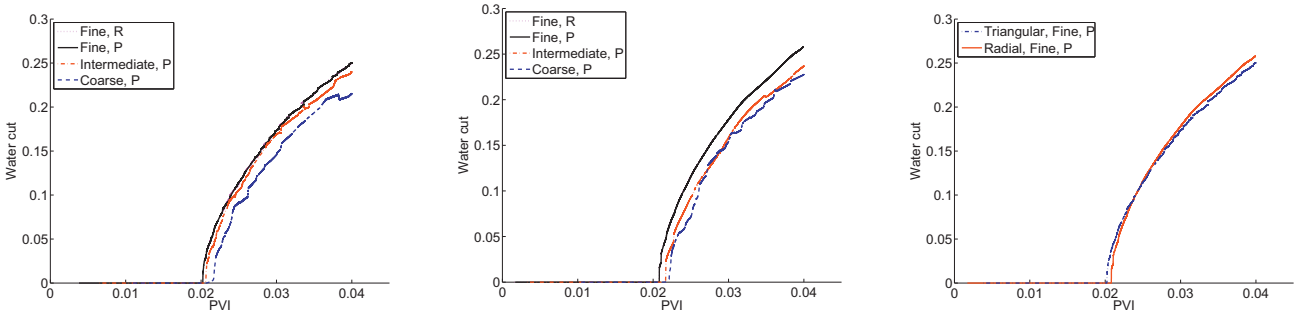

(a) Local triangular grid. (b) Local radial grid. (c) Fine triangular and radial grid.

Fig. 22: Water cuts for both near-well grids at three different refinement levels. The water cut obtained from a reference space discretization is shown for the fine grid only. Observe that the fine grid water cut curves for the discretization in $\mathcal{R}$ and $\mathcal{P}$ are visually indistinguishable. The triangular grid exhibits an earlier breakthrough time than the radial grid at all levels, and seems to be closer to convergence. The water production rates are fairly similar for the two near-well grids.

almost identical. This applies to both choices of local grids. Also, for both grids, the water breakthrough occurs at an earlier time for finer grids. However, for all refinement levels, the triangular grid exhibits an earlier breakthrough time than the radial grid. The triangular grid seems closer to convergence.

However, the water production rates appear to be fairly similar for the two different near-well grids.

6 Concluding Remarks

In this work, we have compared the numerical convergence behavior of control-volume MPFA schemes on anisotropic, heterogeneous near-well problems. The simulations are performed using flexible near-well grids which are adapted to the known logarithmic pressure variation in the near-well flow. We have employed triangular and radial near-well grids. The schemes have been tested for different anisotropy ratios. We have shown that the much-used two-point scheme does not converge for anisotropic problems. Furthermore, we have found that the MPFA schemes exercise deteriorated convergence behavior for equidistant near-well grids. The convergence rates for various MPFA schemes on logarithmically refined grids are given. The pressure exhibits quadratic convergence for both near-well grids. This applies to discretization both in physical space and reference space. The normal velocity is seen to have the same convergence behavior as the pressure for the local radial grid, whereas for the triangular grid, we expect the asymptotic rate of convergence to reach h^2. Moreover, we have seen that the rates of convergence do not seem to depend on the choice of discretization space. Thus, for the sake of simplicity, we may argue that a discretization in physical space is preferable. The numerical results also indicate that a triangular grid, due to a smaller error, should be preferred over a radial grid. The flexible nature of the triangular grid will probably be even more beneficial for more complex near-well flow. Finally, we have shown a way to couple the near-well grids with a surrounding global grid.

The near-well models are also applied in simulations of a two-phase flow problem. These results support the observations from the single phase experiments regarding the choice of discretization space. A discretization in physical space seems to be the reasonable choice. Further, there are some disparities between the saturation profiles stemming from a local radial grid and a local triangular grid, respectively. And due to the lack of proper analytical solutions, we have no means to conclude which near-well grid yields the more reliable simulations. However, the disparities between the different grids do not seem to be significant. This is especially seen in the water breakthrough times. Thus, both approaches are seen to yield good results.

For heterogeneous and anisotropic media, it is well-known that MPFA methods can yield solutions with spurious oscillations, see, e.g., [24,25] . These monotonicity issues are most likely to occur in regions where the solutions are strongly non-linear. The logarithmic pressure variation in the well vicinity can thus be expected to trigger such oscillatory behavior. However, we have not observed any monotonicity problems in our simulations. By construction, MPFA methods are exact for linear pressure fields, and they are also well suited

to capture nearly linear behavior. Here, the near-well grids are adapted to the non-linearity by a logarithmic refinement radially, rendering a nearly constant pressure drop between adjacent cells in the radial direction. This can explain the non-oscillatory behavior of our near-well solutions.

The results of this work are based on local grid refinement in the near-well region. This yields a good resolution the nature of the well flow. However, for full-scale simulations involving several wells, it may not be reasonable to employ such computationally expensive techniques in a small part of the reservoir. Moreover, fine grids yield impractical CFL-restrictions on the time steps. Future challenges involve development of strategies to overcome this issue. Also, the simulations here are for simple 2D two-phase flow, a natural extension will include 3D three-phase flow for more complex physical processes.

Acknowledgements We would like to thank the reviewers for valuable feedback.

References

1. I. Aavatsmark. An introduction to multipoint flux approximations for quadrilateral grids. *Comput. Geosci.*, 6(3-4):405–432, 2002.
2. I. Aavatsmark. Interpretation of a two-point flux stencil for skew parallelogram grids. *Comput. Geosci.*, 11(3):199–206, 2007.
3. I. Aavatsmark, T. Barkve, Ø. Bøe, and T. Mannseth. Discretization on unstructured grids for inhomogeneous, anisotropic media. I. Derivation of the methods. *SIAM J. Sci. Comput.*, 19(5):1700–1716, 1998.
4. I. Aavatsmark, T. Barkve, Ø. Bøe, and T. Mannseth. Discretization on unstructured grids for inhomogeneous, anisotropic media. II. Discussion and numerical results. *SIAM J. Sci. Comput.*, 19(5):1717–1736, 1998.
5. I. Aavatsmark, G. T. Eigestad, and R. A. Klausen. Numerical convergence of the MPFA for general quadrilateral grids in two and three dimensions. In D. N. Arnold, P. B. Bochev, R. B. Lehoucq, R. A. Nicolaides, and M. Shaskov, editors, *Compatible spatial discretizations*, volume 142 of *IMA Vol. Math. Appl.*, pages 1–21. Springer, New York, 2006.
6. I. Aavatsmark, G. T. Eigestad, B. T. Mallison, and J. M. Nordbotten. A compact multipoint flux approximation method with improved robustness. *Numer. Methods Partial Diff. Eqns.*, 24:1329–1360, 2008.
7. Y. Brennier and J. Jaffré. Upstream differencing for multiphase flow in reservoir simulation. *SIAM J. Numer. Anal.*, 28(3):685–696, 1991.
8. Y. Cao, R. Helmig, and B. I. Wohlmuth. Geometrical interpretation of the multi-point flux approximation L-method. *Int. J. Numer. Methods Fluids*, 60(11):1173–1199, 2008.
9. Q.-Y. Chen, J. Wan, Y. Yang, and R. T. Mifflin. Enriched multi-point flux approximation for general grids. *J. Comp. Phys.*, 227:1701–1721, 2008.
10. Z. Chen, G. Huan, and Y. Ma. *Computational Methods for Multiphase Flows in Porous Media*. Computational Science & Engineering. SIAM, Philadelphia, PA, 2006. ISBN 0-89871-606-3.
11. Y. Ding and L. Jeannin. A new methodology for singularity modelling in flow simulations in reservoir engineering. *Comput. Geosci.*, 5:93–119, 2001.
12. Y. Ding and L. Jeannin. New numerical schemes for near-well modeling using flexible grids. *SPE J.*, 9(1):109–121, 2004. SPE 87679.
13. T. A. Driscoll. Algorithm 843: Improvements to the Schwarz-Christoffel toolbox for Matlab. *ACM Trans. Math. Soft.*, 31(2):239–251, 2005.
14. M. G. Edwards. Unstructured, control-volume distributed, full-tensor finite-volume schemes with flow based grids. *Comput. Geosci.*, 6(3-4):433–452, 2002.
15. M. G. Edwards and C. F. Rogers. Finite volume discretization with imposed flux continuity for the general tensor pressure equation. *Comput. Geosci.*, 2(4):259–290, 1998.
16. M. G. Edwards and H. Zheng. A quasi-positive family of continuous Darcy-flux finite-volume schemes with full pressure support. *J. Comput. Phys.*, 227:9333–9364, 2008.
17. H. A. Friis, M. G. Edwards, and J. Mykkeltveit. Symmetric positive definite flux-continuous full-tensor finite-volume schemes on unstructured cell-centred triangular grids. *SIAM J. Sci. Comput.*, 31(2):1192–1220, 2008.
18. E. Keilegavlen and I. Aavatsmark. Monotonicity for MPFA-methods on triangular grids. *Submitted to Comput. Geosci.*, 2009.
19. R. A. Klausen, F. A. Radu, and G. T. Eigestad. Convergence of MPFA on triangulations and for Richards' equation. *Int. J. Numer. Methods Fluids*, 58:1327–1351, 2008.
20. R. A. Klausen and R. Winther. Robust convergence of multipoint flux approximation on rough grids. *Numer. Math.*, 104(3):317–337, 2006.
21. J. V. Lambers, M. G. Gerritsen, and B. T. Mallison. Accurate local upscaling with variable compact multipoint transmissibility calculations. *Comput. Geosci.*, 12(3):399–416, 2008.
22. M. J. Mlacnik and Z. E. Heinemann. Using well windows in full-field reservoir simulation. *SPE Res. Eval. & Engrg.*, 6:275–285, 2003. SPE 85709.
23. S. Mundal, D. A. DiPietro, and I. Aavatsmark. Compact-stencil MPFA method for heterogeneous highly anisotropic second-order elliptic problems. In R. Eymard and J.-M. Hérard, editors, *Finite Volumes for Complex Applications V*, pages 905–918. Wiley, 2008.
24. J. M. Nordbotten and I. Aavatsmark. Monotonicity conditions for control volume methods on uniform parallelogram grids in homogeneous media. *Comput. Geosci.*, 9(1):61–72, 2005.
25. J. M. Nordbotten, I. Aavatsmark, and G. T. Eigestad. Monotonicity of control volume methods. *Numer. Math.*, 106(2):255–288, 2007.
26. D. W. Peaceman. Interpretation of well-block pressures in numerical reservoir simulation. *SPE J.*, 18(3):183–194, 1978. SPE 6893.
27. D. W. Peaceman. Interpretation of well-block pressures in numerical reservoir simulation with nonsquare grid blocks and anisotropic permeability. *SPE J.*, 23(3):531–543, 1983. SPE 10528.
28. D. W. Peaceman. Further discussion of productivity of a horizontal well. *SPERE*, pages 437–438, August 1990. SPE 20799.
29. D. W. Peaceman. Further discussion of productivity of a horizontal well. *SPERE*, pages 149–150, February 1991. SPE 21611.
30. O. A. Pedrosa Jr. and K. Aziz. Use of a hybrid grid in reservoir simulation. *SPERE*, 2:611–621, 1986. *Trans.*, AIME, 281. SPE 13507.
31. P.-O. Persson and G. Strang. A simple mesh generator in Matlab. *SIAM Rev.*, 46(2):329–345, 2004.

32. R. Potsepaev, C. L. Farmer, and A. J. Fitzpatrick. Multi-point flux approximation via upscaling. *SPE Reservoir Simulation Symposium*, 2009. SPE 118979.
33. G. Strang and G. J. Fix. *An Analysis of the Finite Element Method*. Prentice-Hall, 1973.
34. C. Wolfsteiner and L. J. Durlofsky. Near-well radial upscaling for the accurate modeling of nonconventional wells. SPE Western Regional/AAPG Pacific Section Joint Meeting, Anchorage, Alaska, May 2002. SPE 76779.